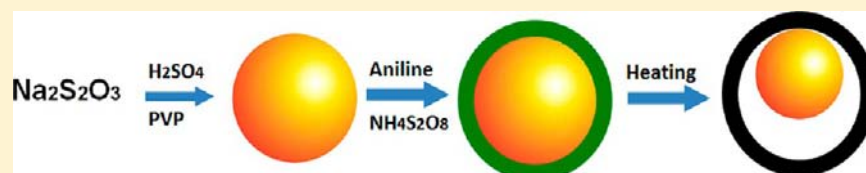


Yolk–Shell Structure of Polyaniline-Coated Sulfur for Lithium–Sulfur Batteries

Weidong Zhou,^{*,†,‡,§} Yingchao Yu,^{†,‡} Hao Chen,[†] Francis J. DiSalvo,[†] and Héctor D. Abruña^{*,†}

[†]Department of Chemistry and Chemical Biology, Cornell University, Ithaca, New York 14853, U.S.A.

S Supporting Information



ABSTRACT: Lithium–sulfur batteries have attracted much attention in recent years due to their high theoretical capacity of 1672 mAh g⁻¹ and low cost. However, a rapid capacity fade is normally observed, attributed mainly to polysulfide dissolution and volume expansion. Although many strategies have been reported to prolong the cyclability, the high cost and complex preparation processes still hinder their practical application. Here, we report the synthesis of a polyaniline–sulfur yolk–shell nanocomposite through a heating vulcanization of a polyaniline–sulfur core–shell structure. We observed that this heating treatment was much more effective than chemical leaching to prepare uniform yolk–shell structures. Compared with its sulfur–polyaniline core–shell counterparts, the yolk–shell nanostructures delivered much improved cyclability owing to the presence of internal void space inside the polymer shell to accommodate the volume expansion of sulfur during lithiation. The yolk–shell material exhibited a stable capacity of 765 mAh g⁻¹ at 0.2 C after 200 cycles, representing a promising future for industrial scale Li–S batteries.

INTRODUCTION

The widespread usage of portable electronic devices and the rapid growth of electric vehicles require the development of next-generation batteries with higher capacity and energy density. Among all rechargeable batteries, the lithium–sulfur (Li–S) cell is one of the most promising candidates due to: (1) it has a high theoretical capacity of 1672 mAh g⁻¹, which is over 5 times that of currently used transition metal oxide cathode materials; (2) it is low cost and there are abundant resources of sulfur; (3) it is nonpoisonous and environmentally benign.^{1–5} Despite these advantages, the practical application of Li–S cells is still limited mainly due, at least in part, to: (1) the low conductivity of sulfur (5 × 10⁻³⁰ S cm⁻¹ at 25 °C); (2) the dissolution of polysulfides and the resulting shuttling effect in the charge–discharge process; (3) the volumetric expansion during the discharge of the cell.^{4–8} While the dissolution of polysulfides is the hardest problem to overcome, these issues often accompany each other. Therefore, a systematic material design strategy intended to prevent polysulfide dissolution might address all these three problems at once.

The high capacity and cycling ability of sulfur arises from the electrochemical cleavage and re-formation of sulfur–sulfur bonds in the cathode, which is believed to proceed in two steps. First, the reduction of sulfur to lithium higher polysulfides (Li₂S_{*n*}, 4 ≤ *n* ≤ 8) is followed by further reduction to lithium lower polysulfides (Li₂S_{*n*}, 1 ≤ *n* ≤ 3).^{6–8} The higher polysulfides are easily dissolved into the organic liquid electrolyte, enabling them to penetrate through the polymer separator and react with the lithium metal anode, leading to the

loss of sulfur active materials. Even if some of the dissolved polysulfides could diffuse back to the cathode during the recharge process, the sulfur particles formed on the surface of the cathode are electrochemically inactive owing to the poor conductivity. Such a degradation path leads to poor capacity retention, especially during the long cycling (i.e., more than 100 cycles).

Efforts to trap the sulfur have mainly focused on the use of mesoporous carbons to absorb polysulfides through weak intermolecular interactions^{9–17} and physically encapsulating sulfur particles with conducting polymers^{18–24} or graphite carbon.^{25–29} The mesoporous carbon/sulfur composites are often prepared via the sulfur vapor impregnation into conductive mesoporous carbons, which show obvious advantages on their high conductivity and large surface area due to the small pore size and large overall pore volume. However, if the sulfur can diffuse into the small pores of the mesoporous carbons, it could also diffuse out theoretically, considering the fact that the sulfur can still be accessed by an electrolyte for extended duration. Although the weak interactions between sulfur and the mesopores could alleviate the dissolution of polysulfides in the short term, the polysulfides could still eventually be dissolved. This is likely the reason why extended cycle life (>100 cycles) tests, with stable capacity retention and high Coulombic efficiency, are rarely reported for this type of composite. On the other hand, the methodology of core–shell

Received: September 13, 2013

Published: October 10, 2013

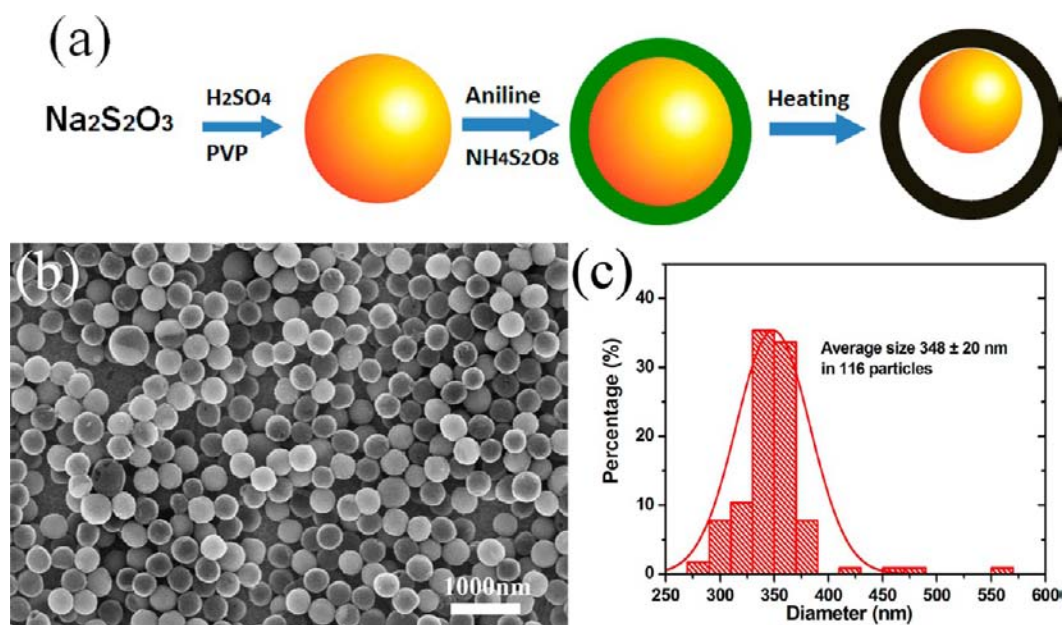


Figure 1. (a) Two-step synthesis route for a S–Pani composite, with the yellow sphere representing sulfur, the dark green shell representing polyaniline, and the black shell representing vulcanized polyaniline. (b) SEM images of the S–Pani core–shell composite using H_2SO_4 as the acid source and (c) the particle size distribution.

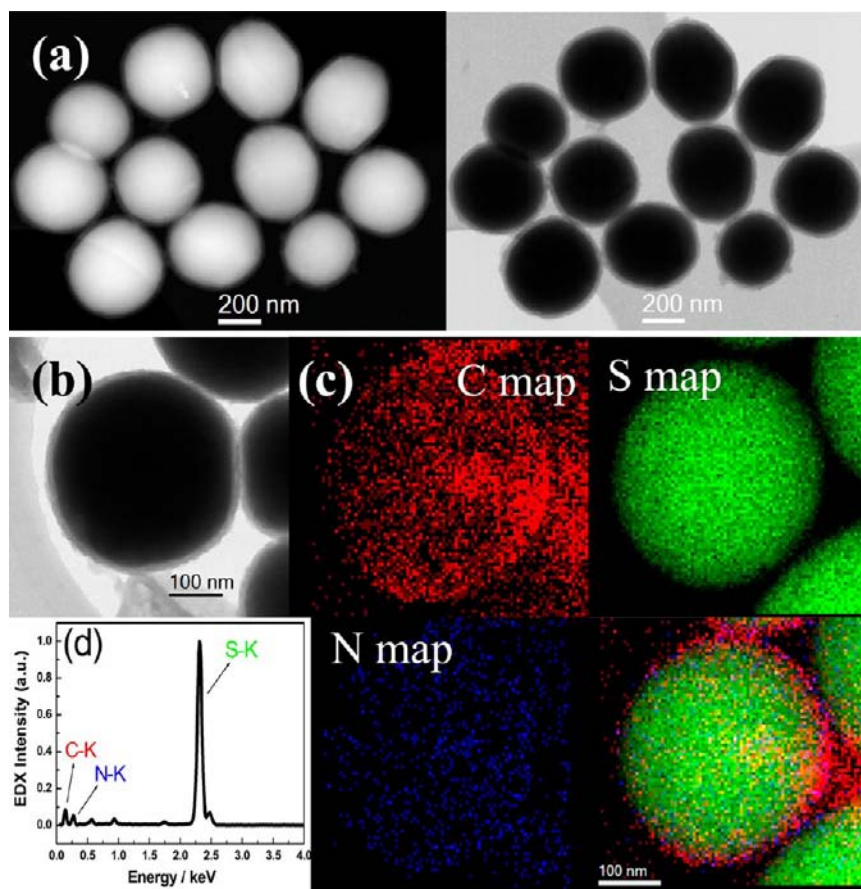


Figure 2. (a) HAADF- and BF-STEM images of S–Pani core–shell structure. (b) Magnified image of a single S–Pani core–shell particle and (c) the corresponding EDX elemental mapping of carbon, sulfur, and nitrogen, along with an overlay of those three maps, showing the enrichment of carbon and nitrogen on the shell. (d) EDX spectrum of S–Pani core–shell composite.

composites adopts the reverse order, in which sulfur nanoparticles are first prepared and then coated with a conductive

polymer or graphite carbon. While this method could provide for the long-term retention of sulfur, the large volumetric

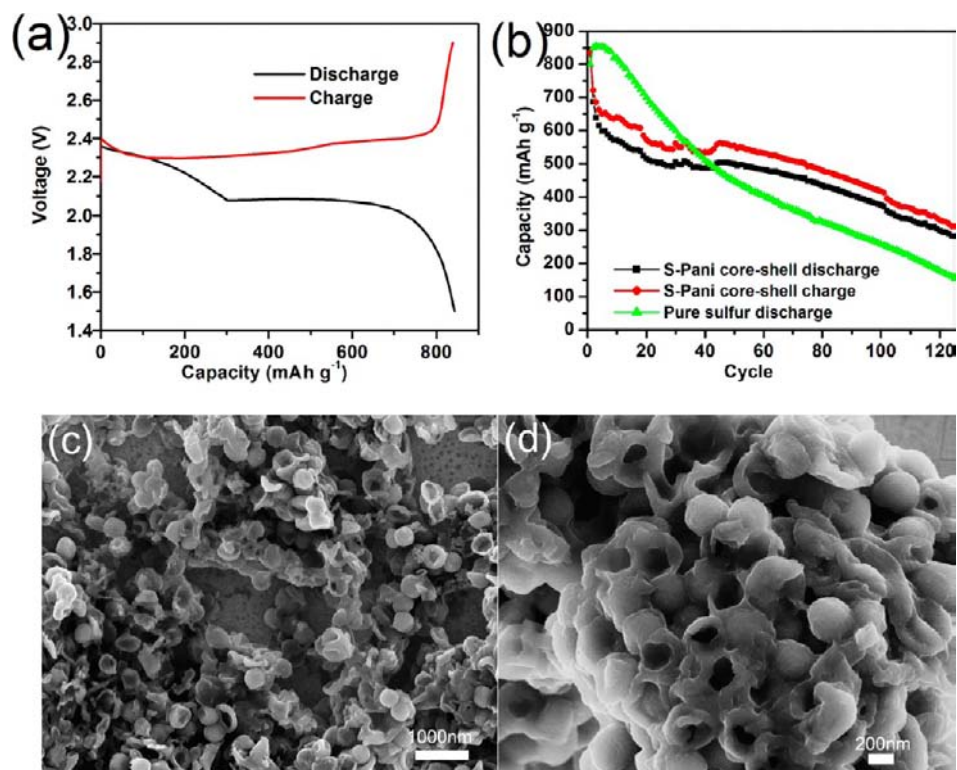


Figure 3. (a) Charge/discharge profiles and (b) charge/discharge capacities vs cycle number for a S–Pani core–shell cathode at a rate of 0.2 C ($1\text{ C} = 1672\text{ mA g}^{-1}$). The capacity values were calculated on the basis of the mass of sulfur. Large scale (c) and magnified (d) SEM images of S–Pani core–shell composites after running five cycles in coin cells.

expansion of sulfur during lithiation renders the protective coating layer susceptible to cracking or even breaking, resulting in the loss of polysulfides. In this respect, Cui and co-workers pioneered the concept of forming a yolk–shell structure to adjust the amount of sulfur encapsulated inside the TiO_2 shell, leaching only a fraction of the encapsulated sulfur using organic solvents.³⁰ This approach greatly improved the confinement of sulfur, resulting in a long-term cycling performance for Li/S batteries. Despite the promising progress, some issues remain; for example, the electrolyte might still dissolve away additional polysulfides, considering the fact that toluene could dissolve out the sulfur during the preparation of this system. It is difficult to control the amount of sulfur that leaches while maintaining a uniform distribution of leaching percentage across an entire array of nanoparticles. The insulating nature of the TiO_2 shell in the electrochemical window of 1.5 to 3.0 V versus Li can limit the actual capacity of the sulfur. Another principle phenomenon in Li/S batteries is that polyvinylidene fluoride (PVDF) dissolved in *N*-methyl-2-pyrrolidone (NMP) was generally employed as the binder. However, NMP could dissolve sulfur out of the preconstructed nanostructures, and the evaporation of NMP under vacuum could also cause related environmental problems.³¹

In this paper, sulfur–polyaniline (S–Pani) core–shell and yolk–shell nanoarchitectures have been prepared, tested, and compared. They exhibited different cycling stability, especially in prolonged cycling performance. The yolk–shell nano-composite was prepared through a heating treatment of the core–shell composite and was found to provide higher capacity retention, owing to its unique morphology that encapsulated the sulfur inside the polymer shells with a buffer void. The advantage of yolk–shell structures lies in the presence of

internal void space to accommodate the volumetric expansion of sulfur during lithiation, thus preserving the structural integrity of the shell while minimizing polysulfide dissolution. With the help of this yolk–shell structure, the capacity of Li/S batteries could be stabilized at 765 mAh g^{-1} at 0.2 C and 628 mAh g^{-1} at 0.5 C after 200 cycles.

RESULTS AND DISCUSSION

The S–Pani core–shell structure was synthesized as shown in Figure 1. First, the monodispersed sulfur nanoparticles were prepared through the reaction of sodium thiosulfate with acid (HCl , HCOOH , and H_2SO_4 were tested) in the presence of 1% (weight ratio) polyvinylpyrrolidone (PVP, $M_w \sim 40\,000$).^{32,33} The freshly prepared sulfur particles were then dispersed in an aqueous solution of aniline and diluted sulfuric acid under strong stirring. The polyaniline-coated sulfur could be obtained through oxidation with ammonium persulfate at $0\text{ }^\circ\text{C}$ for 24 h.^{34,35} The scanning electron microscopy (SEM) image in Figure 1 shows uniform spherical nanoparticles prepared using H_2SO_4 as the acid source, with an average diameter of $348 \pm 20\text{ nm}$. When HCl and HCOOH were employed as the acid sources, the obtained nanoparticles showed not only larger but also nonuniform nanoparticles, as shown in the Supporting Information (SI) Figure S1. Comparisons of maximum particle size obtained in the presence of 1% PVP show the following order: $\text{H}_2\text{SO}_4 < \text{HCOOH} < \text{HCl}$. The surface of S–Pani particles appears to be very rough, with many nanoparticles protruding on the surface (SI, Figure S2), which can be attributed to the cross aggregation of polyaniline chains. The high angle annular dark field and bright field scanning transmission electron microscopy (HAADF-STEM, BF-STEM) images indicated that sulfur nanoparticles were

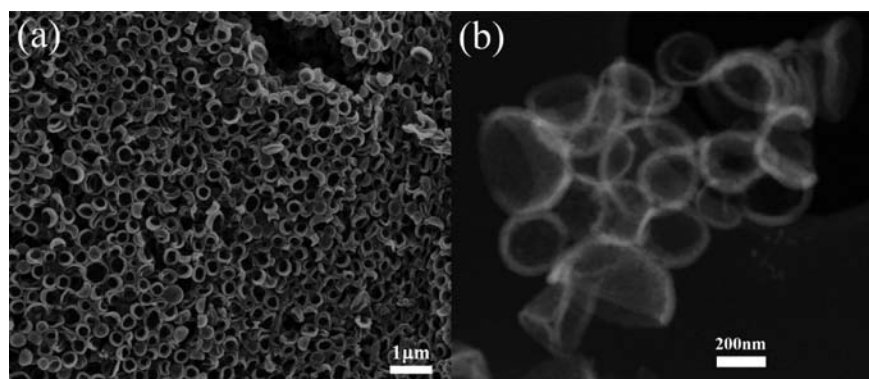


Figure 4. (a) SEM and (b) HAADF-STEM images of S-Pani core-shell structure after leaching in toluene/ethanol.

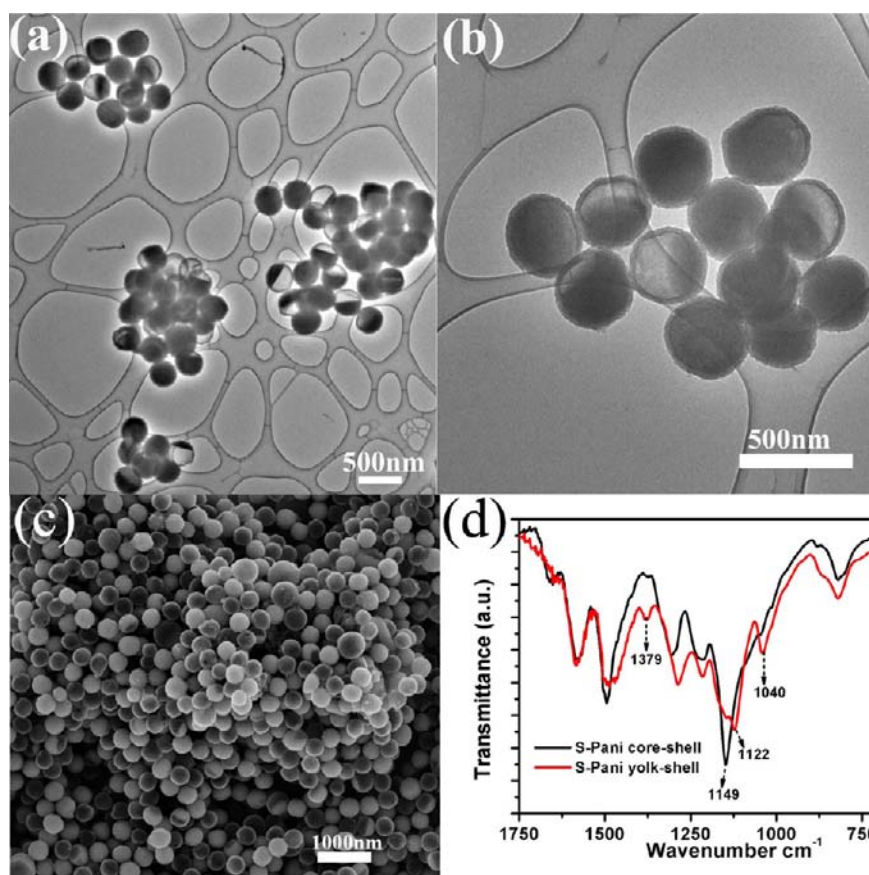


Figure 5. (a) Large-scale TEM image, (b) magnified TEM image, and (c) SEM image of S-Pani yolk-shell structures after heat treatment. (d) FTIR spectra of S-Pani core-shell and yolk-shell structures.

uniformly encapsulated inside the polyaniline shell. From the contrast variation in Figure 2a,b, the polyaniline shell was measured to be about 15 nm, whereas the sulfur core was about 300 nm. Energy dispersive X-ray (EDX) elemental mapping confirmed that the core of the particle in Figure 2b was sulfur, along with overlaying carbon and nitrogen signals from coating polyaniline shells (Figure 2c). The EDX spectrum displayed a very strong sulfur peak, which was over 10-fold higher in peak intensity relative to carbon, as shown in Figure 2d. The X-ray diffraction (XRD) data of this S-Pani core-shell structure only gave the well-matched signals of orthorhombic sulfur, as shown in the Figure S3 of SI, indicating that the polyaniline was amorphous. Thermogravimetric analysis (TGA) showed that about 82 wt % of sulfur was incorporated in the S-Pani

composite (SI, Figure S4). Compared with recent reports on the polymer-coated sulfur composites with a particle diameter of over 1 μm ,^{21,22,36,37} the sulfur particles' diameter of 300 nm in this study was much smaller, which would facilitate both the ionic transportation of Li^+ and the electrochemical availability efficiency of sulfur, owing to the poor conductivity of sulfur.

We prepared cells in which the S-Pani core-shell composite was used as the cathode and lithium foil was used as the anode; additionally, 1.0 M lithium bis-trifluoromethanesulfonylimide (LiTFSI) in a mixed solvent of 1,3-dioxolane and 1,2-dimethoxyethane (DOL/DME, 1:1, v/v) containing LiNO_3 (1 wt %) was used as the electrolyte. S-Pani was mixed with carbon black (Super P) and water-soluble binder sodium alginate (80:15:5 by weight) to prepare the cathode film.³⁸

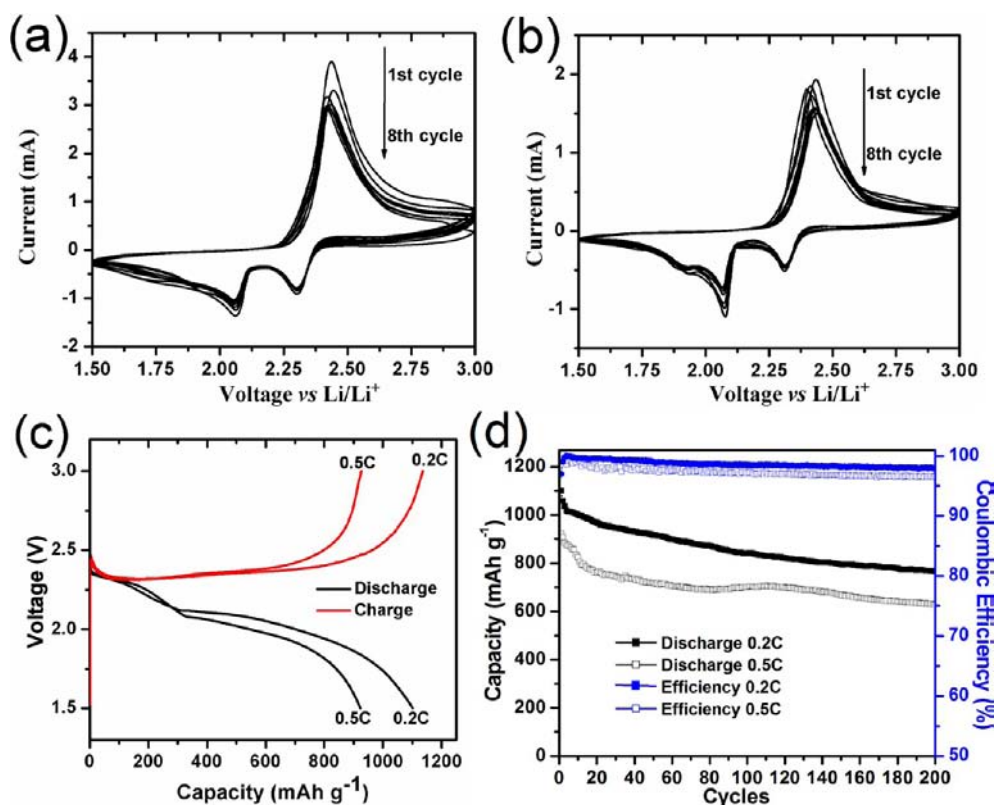


Figure 6. Typical CV curves of S–Pani yolk–shell cathode at a sweep rate of 0.05 mV s⁻¹ (a) and 0.02 mV s⁻¹. (b) Charge/discharge profiles and capacities vs cycle number for S–Pani yolk–shell composite cathodes at a rate of 0.2 C (c) and 0.5 C (d).

Here, water-soluble binder was employed to avoid unwanted dissolution of sulfur or even the damage of the nanostructures. As shown in Figure 3a, two well-defined discharge plateaus were observed, which could be assigned to the multistep reduction mechanism of elemental sulfur, as reported previously.^{6–8} The first plateau, centered around 2.35 V, was generally attributed to the reduction of the S₈ ring and the formation of S₈²⁻. The discharge plateau at 2.08 V was ascribed to the further reduction of the higher polysulfides (Li₂S_n, 4 ≤ n ≤ 8) to the lower polysulfides (Li₂S_n, n ≤ 3). Within the first 20 cycles, the capacity showed clear fading with cycling, followed by a relatively stable capacity from the 20th to the 50th cycle. These features were similar to the previous reports,^{22,36} where only the first 50 cycles were presented. In longer cycling, the capacity dropped heavily from 510 to 280 mAh g⁻¹ after 125 cycles, indicating that the core–shell structure was not effective in preventing the long-term loss of sulfur into the electrolyte during the redox processes. In comparison, a control electrode based on pure sulfur suffered from a much faster capacity fade, yielding a capacity of only 124 mAh g⁻¹ after 125 cycles. These results indicate that although the core–shell structure provides a protective coating, its integrity is not preserved during the volumetric expansion, and polysulfides eventually escape during the discharge process. The SEM image of the S–Pani core–shell composite after running five cycles in coin cells gave visualized evidence, in which around half of the particles were broken or shrunk (shown in Figure 3c,d). All these above results indicated that the polyaniline shell could not effectively accommodate the large volumetric expansion during the lithiation process, especially in the long-term and repeating discharge–charge processes.

In order to provide more space to allow for the volume expansion of sulfur particles during lithiation, it is desirable to develop a S–Pani yolk–shell nanocomposite with polyaniline shells and tunable buffer voids. In this respect, the strategy of leaching sulfur out of the core–shell structures through partial dissolution of sulfur in toluene has been reported.³⁰ However, if the toluene can leach out the sulfur, it is also plausible that the electrolyte solvent DOL/DME could leach out the polysulfides during the discharge–charge process. To verify this, we tried to prepare the S–Pani yolk–shell nanocomposites by leaching them with toluene/ethanol. As predicted, all of the core–shell structures were broken and the resulting half-bowl structures were observed, as shown in images of the Figure 4a. The STEM image showed that there was almost no sulfur left in the half-bowl structures (Figure 4b), which indicates that nanosize sulfur was easily dissolved under these conditions, and the polyaniline shells were subsequently collapsed.

From recent studies on polyaniline-doped sulfur for Li/S electrode composites, polyaniline could react with sulfur at high temperature to form a cross-linked structure, which significantly improved the cycling performance.^{39,40} With this knowledge in mind, the S–Pani core–shell composites were heated at 180 °C in a sealed tube filled with argon for 12 h, with the expectation that elemental sulfur would react with polyaniline shell to form a three-dimensional, cross-linked S–Pani yolk–shell structure with both inter- and/or intrachain sulfide and/or disulfide bonds interconnection through in situ vulcanization.³⁹ Such a S–Pani yolk–shell structure could potentially help to provide buffer void space for the volumetric expansion of the polysulfides during lithiation and physically confine the elemental sulfur and the polysulfides.

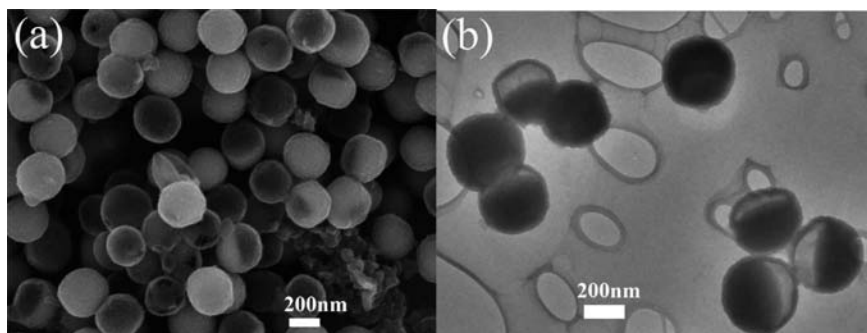


Figure 7. The SEM (a) and TEM (b) images of S-Pani yolk-shell structures after the fifth charge in the coin cell. Small particles are the carbon black particles.

Transmission electron microscopy (TEM) and SEM images of S-Pani after heat treatment exhibited uniform, yolk-shell structures without any broken shell, as shown in Figure 5. The intact polymer shell was well-preserved and, partially hollowed yolk-shell structures of the S-Pani could clearly be observed. The void space appeared as either an empty area or lower intensity area due to the two-dimensional projection nature of the TEM images.⁴¹ The ability of sulfur vapor to diffuse out through the polyaniline shell indicates the porous nature of polyaniline shells, which can be ascribed to the cross aggregation of polyaniline chains. Unlike what the S-Pani core-shell structure did in the toluene/ethanol, the polyaniline shell did not shrink with the diffusing out of the sulfur in the heating treatment, suggesting that the mechanical strength of polyaniline shell was enhanced during the heating vulcanization. It can be attributed to the cross-linked sulfide and/or disulfide bonds interconnection among polyaniline chains. To verify it experimentally, Fourier transformed infrared (FTIR) spectra of the S-Pani core-shell and heat-treated yolk-shell structures were recorded and shown in Figure 5d. Both the C=C stretching vibration at 1497 cm^{-1} from the benzenoid rings and the C-N stretching vibrational bands at 1379 , 1122 , and 1040 cm^{-1} arose in the heat-treated S-Pani yolk-shell composites, which could be assigned to the vibration of C-S.⁴²⁻⁴⁴ The intensity of the C-H vibrational band in the vicinity of 1149 cm^{-1} significantly weakens, further confirming the replacement of H atoms on aromatic rings by S atoms.³⁹ Furthermore, the heat-treated S-Pani yolk-shell composites showed a blacker color compared with the dark green of the S-Pani core-shell composites, as shown in Figure S5 of SI. In contrast to the orthorhombic sulfur of the S-Pani core-shell composite, the XRD of heat-treated S-Pani yolk-shell composite indicated that it contained two types of sulfur, the sulfur (orthorhombic) and Rosickyite (monoclinic), as shown in Figure S6. Rosickyite is a polymorph of sulfur and could be obtained through crystallization at high temperature. These features confirm that elemental sulfur reacted with the unsaturated bonds of polyaniline during the heat treatment through a well-known vulcanization reaction. The sulfur content was found to be about 58% in the heat-treated yolk-shell composites according to the TGA result in Figure S7 of SI, which was around 46.4% in the whole electrode films, considering 20% of carbon black and binder. The formation of the yolk-shell structure could be attributed to the vulcanizing reaction and partial evaporation of the elemental sulfur during the heating treatment.

Cyclic voltammograms (CVs) of a Li-S cell with a heat-treated S-Pani yolk-shell cathode were obtained at a scan rate of 0.05 and 0.02 mV s^{-1} (Figure 6a,b). Two reduction peaks around 2.35 and 2.08 V were observed and could be assigned to the multistep reduction mechanism of elemental sulfur, as reported previously.⁶⁻⁸ Compared with typical CV curves of a Li-S cell, the reduction peak of the heat-treated S-Pani yolk-shell cathode at 2.08 V was a little smaller, and a shoulder centered at 1.9 V could be clearly observed, especially at a slow scan rate. Also, the reduction peak at 1.9 V could be observed in every reduction cycle of the CV curves from Figure 6a,b, indicating that the reduction at 1.9 V was reproducible. This reduction peak could be attributed to the reduction of disulfide bonds connected with polyaniline through the vulcanization.⁴⁰ Figure 6c shows the discharge-charge profiles of coin cells using heat-treated S-Pani yolk-shell composites as the cathode materials at different current densities. Unlike the two clear discharge plateaus of the S-Pani core-shell composite electrode, two less-well-defined discharge plateaus centered around 2.35 and 2.08 V were observed for heat-treated S-Pani yolk-shell composites, which was in high agreement with the CV curves of Figure 6a.^{39,40} As illustrated in Figure 6c, the heat-treated S-Pani yolk-shell composites showed an initial capacity of 1101 and 920 mAh g^{-1} under different current densities of 0.2 and 0.5 C , respectively. Although there was an initial capacity drop, the capacity tended to stabilize after about 10 cycles at both 0.2 and 0.5 C (Figure 6d). Compared to the S-Pani core-shell electrode described earlier, the heat-treated yolk-shell composite electrode exhibited significantly improved capacity retention with cycling, which could be ascribed to the combined contributions from the buffer space and stabilized shell through vulcanization. After cycling for 200 cycles, a discharge capacity of 765 mAh g^{-1} was obtained at 0.2 C , which corresponded to a 69.5% capacity retention. At a higher current density of 0.5 C , a stable cycling performance was observed with a capacity around 628 mAh g^{-1} and a 68.3% capacity retention after running 200 cycles. The relatively lower cycling performance at 0.5 C can be attributed, at least in part, to the lower Coulombic efficiency at this current density. The improved cycling stability verifies that the yolk-shell structure can help to immobilize the polysulfides and mitigate capacity fading. To further investigate the stability of the yolk-shell structure during the cycling of coin cells, a cell was disassembled after running five cycles, and the composite was regained after rinsing with water. As shown in the Figure 7, the intact polyaniline shells were still preserved, which suggests that the shell of vulcanized polyaniline can accommodate the volumetric expansion during the charge/discharge process.

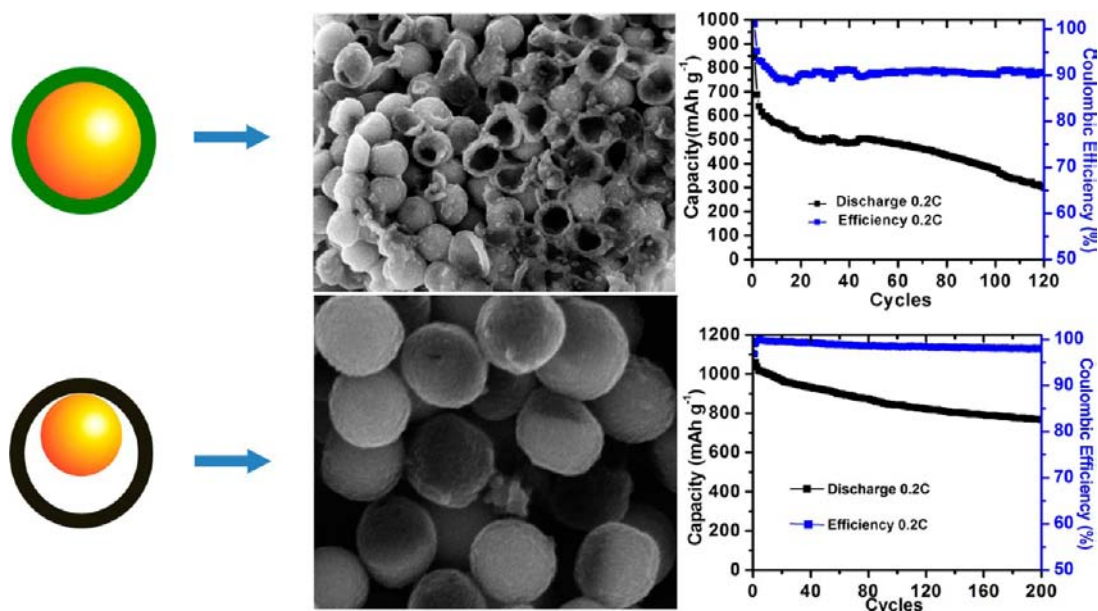


Figure 8. Schematic comparison of the S–Pani core–shell and yolk–shell SEM images after running five cycles in cells and the long-term cycling performance.

During the discharge process, the elemental sulfur was first reduced due to its relatively higher reduction potential. With the reduction of elemental sulfur, that is, the lithiation process, the volume of the sulfur/sulfide species was increased to near twice, which will fill the void space within the shell. After that, the disulfide bonds among polyaniline chains were reduced, and the shell should not shrink much due to the volumetric increase of the inside sulfide species during lithiation. In a subsequent charge process, the sulfide anions on the polymer chains could be reoxidized to form disulfide again and recover the cross-linked polyaniline shell. Therefore, theoretically these processes should not destroy the yolk–shell structures. Experimentally, the CV curves gave a reproducible reduction shoulder at 1.9 V, which indicates that these processes were reversible. In addition, the SEM and TEM images of the yolk–shell structure after running five cycles gave visible evidence that the structure was well-preserved.

The significantly improved cyclability could be ascribed to the sufficient buffer space in the yolk–shell structures, which allowed for the volume expansion of sulfur. After the heat treatment, the sulfur weight content dropped from 82 to 58%, as shown in the TGA data of Figure S4 and S7 of SI, which indicated that more than 2/3 of the sulfur evaporated or reacted with the polyaniline shells based on the assumption that the weight of polyaniline did not change. Since the weight of polyaniline shells should actually increase by some degree during the vulcanization, the evaporated sulfur would be around or less than 2/3. These data indicate that the volume of empty space within the yolk–shell nanostructures was estimated to be around or near twice the sulfur, which would be enough to accommodate the 80% volumetric expansion during the discharge process without causing the shell to crack.¹⁸ Apparently, these values were supported by the TEM images of Figure 5, in which more than half of the space within the shell was void. Experimentally, the integrity of polyaniline shells was still well-preserved after running five cycles in coin cells, as shown in Figure 8, further confirming that the void buffer space of the yolk–shell structures successfully accommodated the

volumetric expansion. By contrast, most polyaniline shells of the core–shell composite were cracked after running five cycles in coin cells, as shown in Figures 3 and 8. All of these above features verified that internal void space in the yolk–shell nanostructures was sufficient to accommodate the volume expansion of polysulfides during lithiation, thus maintaining the intact shells to minimize the polysulfide dissolution and maximize the capacity retention. One thing we should point out is that although this yolk–shell composite delivered much improved cycling stability compared with the core–shell composite, slow capacity degradation could still be observed. The efficiency was just around 97%–98%, which indicates that the dissolution of polysulfides and the subsequent shuttling effect still did not completely vanish in this condition. In addition, the sulfur ratio in the yolk–shell composite was only around 58%, which limited the overall capacity based on the yolk–shell composite. However, owing to the low cost of widely available polyaniline and the easily scaled-up heating process that could give uniform distribution of leaching percentage across the entire array of nanoparticles, it is potentially scalable for industry manufacturing.

CONCLUSION

In summary, polyaniline-coated sulfur with core–shell and yolk–shell structures have been prepared and investigated to immobilize lithium polysulfides as the cathodes of Li–S cells. Compared with the core–shell composite, the as-synthesized S–Pani yolk–shell composite delivered obviously improved cycling stability. The vulcanized soft polymer shells and yolk–shell structures developed in this study successfully encapsulated the sulfur and polysulfide species within the polymer shell and accommodated the volumetric expansion associated with the lithiation, owing to the presence of internal void space. While slight capacity fading was still observed, we believe that these results provide important insights and novel methodology to confine the sulfur and polysulfides for the future application of Li–S batteries.

■ ASSOCIATED CONTENT**■ Supporting Information**

Experimental details for the material preparation, characterization, and device testing, along with additional supporting data. This material is available free of charge via the Internet at <http://pubs.acs.org>.

■ AUTHOR INFORMATION**Corresponding Authors**

*E-mail: hda1@cornell.edu (H.D.A.).

*E-mail: weidongzhou@gm.com (W.Z.).

Present Address

§General Motors Global Research and Development Center, 30500 Mound Road, Warren, Michigan 48090, U.S.A.

Author Contributions

‡These two authors contributed equally.

Notes

The authors declare no competing financial interest.

■ ACKNOWLEDGMENTS

This work was supported by the Department of Energy through Grant No. DE-FG02-87ER45298, by the Energy Materials Center at Cornell (EMC²), an Energy Frontier Research Center funded by the U.S. Department of Energy, Office of Basic Energy Sciences under Award Number DE-SC0001086. This work made use of the electron microscopy facility of the Cornell Center for Materials Research (CCMR) with support from the National Science Foundation Materials Research Science and Engineering Centers (MRSEC) program (DMR 1120296).

■ REFERENCES

- (1) Whittingham, M. S. *Chem. Rev.* **2004**, *104*, 4271–4301.
- (2) Aricò, A. S.; Bruce, P. G.; Scrosati, B.; Tarascon, J.-M.; Schalkwijk, W. V. *Nat. Mater.* **2005**, *4*, 366–377.
- (3) Guo, Y.; Hu, J.; Wan, L. *Adv. Mater.* **2008**, *20*, 2878–2887.
- (4) Bruce, P. G.; Freunberger, S. A.; Hardwick, L. J.; Tarascon, J.-M. *Nat. Mater.* **2012**, *11*, 19–29.
- (5) Manthiram, A.; Fu, Y.; Su, Y.-S. *Acc. Chem. Res.* **2013**, *46*, 1125–1134.
- (6) Yamin, H.; Gorenshstein, A.; Penciner, J.; Sternberg, Y.; Peled, E. *J. Electrochem. Soc.* **1988**, *135*, 1045–1048.
- (7) Peled, E.; Sternberg, T.; Gorenshstein, A.; Lavi, Y. *J. Electrochem. Soc.* **1989**, *136*, 1621–1625.
- (8) Jin, B.; Kim, J. U.; Gu, H. B. *J. Power Sources* **2003**, *117*, 148–152.
- (9) Jayaprakash, N.; Shen, J.; Moganty, S. S.; Corona, A.; Archer, L. A. *Angew. Chem., Int. Ed.* **2011**, *50*, 5904–5908.
- (10) Liang, C.; Dudney, N. J.; Howe, J. Y. *Chem. Mater.* **2009**, *21*, 4724–4730.
- (11) Zhang, C.; Wu, H.; Yuan, C.; Guo, Z.; Lou, X. W. *Angew. Chem., Int. Ed.* **2012**, *51*, 9592–9595.
- (12) Ji, X.; Lee, K. T.; Nazar, L. F. *Nat. Mater.* **2009**, *8*, 500–506.
- (13) Zhang, B.; Qin, X.; Li, G. R.; Gao, X. P. *Energy Environ. Sci.* **2010**, *3*, 1531–1537.
- (14) Ji, X.; Evers, S.; Black, R.; Nazar, L. F. *Nat. Commun.* **2011**, *2*, 325.
- (15) Schuster, J.; He, G.; Mandlmeier, B.; Yim, T.; Lee, K. T.; Bein, T.; Nazar, L. F. *Angew. Chem., Int. Ed.* **2012**, *51*, 3591–3595.
- (16) Xin, S.; Gu, L.; Zhao, N.; Yin, Y.; Zhou, L.; Guo, Y.; Wan, L. *J. Am. Chem. Soc.* **2012**, *134*, 18510–18513.
- (17) Han, S.-C.; Song, M.-S.; Lee, H.; Kim, H.-S.; Ahn, H.-J.; Lee, J.-Y. *J. Electrochem. Soc.* **2003**, *150*, A889–A893.
- (18) Yang, Y.; Yu, G.; Cha, J. J.; Wu, H.; Vosgueritchian, M.; Yao, Y.; Bao, Z.; Cui, Y. *ACS Nano* **2011**, *5*, 9187–9193.

- (19) Yin, L.; Wang, J.; Yang, J.; Nuli, Y. *J. Mater. Chem.* **2011**, *21*, 6807–6810.
- (20) Wu, F.; Chen, J.; Li, L.; Zhao, T.; Chen, R. *J. Phys. Chem. C* **2011**, *115*, 24411–24417.
- (21) Wu, F.; Chen, J.; Chen, R.; Wu, S.; Li, L.; Chen, S.; Zhao, T. *J. Phys. Chem. C* **2011**, *115*, 6057–6063.
- (22) Fu, Y.-Z.; Manthiram, A. *J. Phys. Chem. C* **2012**, *116*, 8910–8915.
- (23) Su, Y.-S.; Manthiram, A. *Nat. Commun.* **2012**, *3*, 1166.
- (24) Wang, L.; Wang, D.; Zhang, F.; Jin, J. *Nano Lett.* **2013**, *13*, 4206–4211.
- (25) Yin, L.; Wang, J.; Lin, F.; Yang, J.; Nuli, Y. *Energy Environ. Sci.* **2012**, *5*, 6966–6972.
- (26) Guo, J.; Xu, Y.; Wang, C. *Nano Lett.* **2011**, *11*, 4288–4294.
- (27) Guo, J.; Yang, Z.; Yu, Y.; Abruña, H. D.; Archer, L. A. *J. Am. Chem. Soc.* **2013**, *135*, 763–767.
- (28) Zheng, G.; Zhang, Q.; Cha, J. J.; Yang, Y.; Li, W.; She, Z. W.; Cui, Y. *Nano Lett.* **2013**, *13*, 1265–1270.
- (29) Lu, S.; Cheng, Y.; Wu, X.; Liu, J. *Nano Lett.* **2013**, *13*, 2485–2489.
- (30) Seh, Z. W.; Li, W.; Cha, J. J.; Zheng, G.; Yang, Y.; McDowell, M. T.; Hsu, P.-C.; Cui, Y. *Nat. Commun.* **2013**, *4*, 1331.
- (31) Schneider, H.; Garsuch, A.; Panchenko, A.; Gronwald, O.; Janssen, N.; Novák, P. *J. Power Sources* **2012**, *205*, 420–425.
- (32) Ji, L.; Rao, M.; Zheng, H.; Zhang, L.; Li, Y.; Duan, W.; Guo, J.; Cairns, E. J.; Zhang, Y. *J. Am. Chem. Soc.* **2011**, *133*, 18522–18525.
- (33) Wang, H.; Yang, Y.; Liang, Y.; Robinson, J. T.; Li, Y.; Jackson, A.; Cui, Y.; Dai, H. *Nano Lett.* **2011**, *11*, 2644–2647.
- (34) Jang, J.; Ha, J.; Lim, B. *Chem. Commun.* **2006**, 1622–1624.
- (35) Liu, Y. D.; Park, B. J.; Kim, Y. H.; Choi, H. J. *J. Mater. Chem.* **2011**, *21*, 17396–17402.
- (36) Li, G.; Li, G.; Ye, S.; Gao, X. *Adv. Energy Mater.* **2012**, *2*, 1238–1245.
- (37) Duan, L.; Lu, J.; Liu, W.; Huang, P.; Wang, W.; Liu, Z. *Colloids Surf., A* **2012**, *414*, 98–103.
- (38) Kovalenko, I.; Zdyrko, B.; Magasinski, A.; Hertzberg, B.; Milicev, Z.; Burtovyy, R.; Luzinov, I.; Yushin, G. *Science* **2011**, *334*, 75–79.
- (39) Xiao, L.; Cao, Y.; Xiao, J.; Schwenzer, B.; Engelhard, M. H.; Saraf, L. V.; Nie, Z.; Exarhos, G. J.; Liu, J. *Adv. Mater.* **2012**, *24*, 1176–1181.
- (40) Zhang, S.; Zhang, L.; Wang, W.; Xue, W. *Synth. Met.* **2010**, *160*, 2041–2044.
- (41) Gu, M.; Li, Y.; Li, X.; Hu, S.; Zhang, X.; Xu, W.; Thevuthasan, S.; Baer, D. R.; Zhang, J.; Liu, J.; Wang, C. *ACS Nano* **2012**, *6*, 8439–8447.
- (42) Yu, X.; Xie, J.; Yang, J.; Huang, H.; Wang, K.; Wen, Z. *J. Electroanal. Chem.* **2004**, *573*, 121–128.
- (43) Aurbach, D.; Pollak, E.; Elazari, R.; Salitra, G.; Kelley, C. S.; Affinito, J. *J. Electrochem. Soc.* **2009**, *156*, A694–A702.
- (44) Diao, Y.; Xie, K.; Xiong, S.; Hong, X. *J. Electrochem. Soc.* **2012**, *159*, A1816–A1821.